Direct experimental observations of the impact of viscosity contrast on convective mixing in a three dimensional porous medium

Rebecca Liyanage,[1, a)] Andrew Russell,[1] John P. Crawshaw,[1] and Sam Krevor[2]

[1)]*Department of Chemical Engineering, Imperial College London, London, UK*

[2)]*Department of Earth Science and Engineering, Imperial College London, London, UK*

(Dated: 15 April 2020)

Analog fluids have been widely used to mimic the convective mixing of carbon dioxide into brine in the study of geological carbon storage. Although these fluids systems had many characteristics of the real system, the viscosity contrast between the resident fluid and the invading front was significantly different and largely overlooked. We used X-ray computed tomography to image convective mixing in a three-dimensional porous medium formed of glass beads and compared two invading fluids which had a viscosity 3.5$\times$ and 16$\times$ that of the resident fluid. The macroscopic behavior such as the dissolution rate and onset time, scaled well with the viscosity contrast. However with a more viscous invading fluid fundamentally different plume structures and final mixing state were observed due in large part to greater dispersion.

[a)]Electronic mail: liyanage.rebecca@gmail.com

I. INTRODUCTION

Convective mixing is a process driven by a density difference between two fluid layers and is an important trapping mechanism in carbon dioxide (CO_2) sequestration[1–3]. As CO_2 dissolves into resident brine, a heavier layer of CO_2 saturated brine accumulates atop the pure brine. The result is an unstable interface where the fresh brine moves upwards due to buoyancy and the heavier CO_2-rich brine sinks creating a convection cell, enhancing the mixing of the two fluids[4].

To study convective mixing experimentally, many researchers have turned to analog fluid pairs to remove the complexities of working at reservoir temperatures and pressures[5–10]. One fluid, in particular, has been used for both 2D and 3D studies of convective mixing. MEG is a mixture of methanol and ethylene glycol that when mixed with water presents with a non-monotonic density mixing curve. The small density difference of the CO_2-brine system that drives the convective mixing process is replicated in these fluids[5,9,10]. More recently, a few studies have attempted to examine convective mixing at conditions that more closely reflect that in the field, particularly by performing experiments using actual CO_2-brine[11] at high-pressure conditions within a porous medium[12–14].

When using model systems to infer real world behaviors it is critical to establish the similarities and differences between the model and reality. Despite the prevalent use of analog systems, it is not clear from the literature that the effects of differences in fluid properties have been fully investigated experimentally. So, here we will investigate one such difference; the viscosity difference between the resident and invading fluid. The viscosity ratio, $M = \mu_2/\mu_1$ evaluates the viscosity of the resident fluid (brine/water, μ_2) to the viscosity of the invading front (CO_2-rich brine/MEG, μ_1). At reservoir conditions, the viscosity difference of CO_2 saturated brine compared to brine has been shown to be negligible[15,16] ($M \approx 1$), but this is not the case for MEG and water at laboratory conditions. In fact, the MEG is 3 times as viscous as the water ($M \approx 0.29$) and represents the inverse situation to the well-known Saffman Taylor problem.

A Saffman Taylor instability is produced when a less viscous fluid invades a more viscous fluid; the front is unstable and characteristic fingers are produced[17,18]. One prominent and recent application is enhanced oil recovery, where a less viscous fluid is injected to mobilize residual oil[19]. As a result viscous fingering has been shown to play a role in enhancing mixing at the interface of two fluids, however, the degree of mixing is highly dependent on the specific viscosity ratio[20]. In particular, it has also been shown that when the invading fluid is more viscous than the

resident fluid, the front usually remains stable[21,22] reducing the mixing potential.

However, in the specific situations where the displacing front is moving slowly enough for the front to become unstable[23–25] it has also been shown numerically that non-linearity in the viscosity profile resulted in reverse fingering. The mixing potential was fundamentally changed in comparison to the linear case [26] for otherwise stable displacements. More recently, it has been found that, a traditionally stable configuration can become unstable if constituent components diffuse at different rates but all contribute to the viscosity. In such a case, a double-diffusive effect is observed [27,28] when the viscosity as a function of dilution or mixing is nonlinear.

Thus far, only a handful of papers have looked at the effect of the viscosity variations in respect to convective mixing specifically. And, of those studies the focus is on the stability of the diffusive boundary layer[29–34] and find that the onset of convection is not only influenced by the viscosity contrast between the invading and defending fluids but also the viscosity of the layer itself. So, there is a clear indication from the literature that the viscosity contrast and the viscosity-dilution curve are non-trivial considerations in fluid-fluid mixing.

However, when analog fluids such as MEG and propylene glycol (PG) have been used to investigate convective mixing, the role of viscosity has been largely overlooked. So, by using 3D experiments, we investigate the interplay between viscosity fingering and buoyancy-driven flow; testing the sensitivity of convective mixing to an increased viscosity contrast between the host fluid and the invading front. The results presented here extend recently published work which focused on convective dissolution using MEG/water[10] and introduces a new, but similar, fluid with a viscosity $4\times$ that of MEG.

II. MATERIALS AND METHODS

Here, we used two fluids pairs, both consisting of an organic solution and water. The first was a mixture of 59% ethylene glycol and 41% methanol, MEG, and the second was a mixture of 65% ethylene glycol and 35% tertiary butanol, BEG (all anhydrous, 99.8%, Sigma-Aldrich). The solutions were subsequently doped with 9 wt% potassium iodide (KI, ReagentPlus®, 99%, Sigma Aldrich) to achieve high X-ray imaging contrast for the experiments. The distilled water was doped with 6 wt% sodium chloride (NaCl, $>$ 99%, Sigma Aldrich) for the MEG and 9 wt% sodium chloride (NaCl, $>$ 99%, Sigma Aldrich) for the BEG.

The density of the pure solutions and their mixtures were measured using an oscillating U-tube

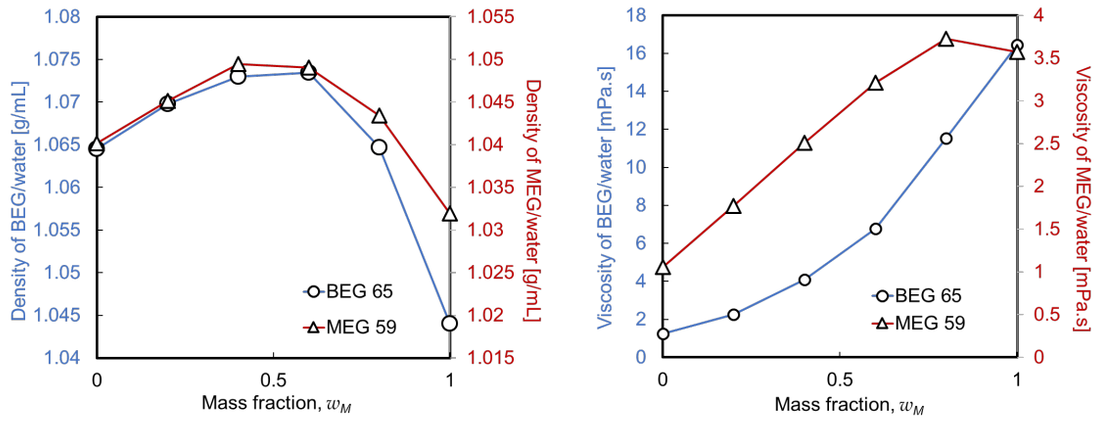

FIG. 1. left: Density curves of the two solution-pairs MEG and BEG (solution 1 with mass fraction w_M) mixed with brine (solution 2 with mass fraction, 1-w_M). The characteristic points on each curve are the maximum density difference achieved upon mixing ($\delta\rho_{max}$), the corresponding weight fraction of the solution ($w^{\max}$) and the point of neutral buoyancy, w^0). The values of these parameters are given in Table I. right: Viscosity curves of the two solution-pairs (solution 1 with mass fraction w_M) mixed with brine (solution 2 with mass fraction, 1-w_M).

density meter (DM5000 by Anton Paar) at 20°C and 1 atm. For each measurement, approximately 3 mL of the solution was used, and the density was taken to be the average of three repeated measurements. The density curves are shown in Figure 1a as a function of the mass fraction of MEG/BEG, w_M. Both MEG and BEG present a characteristic non-monotonic profile with a maximum at intermediate organic fractions ($w_M = 0.4 - 0.5$) and a density larger than that of pure brine, whereas at larger concentrations ($w_M = 0.8 - 0.9$) the solution became buoyant. The exact values are detailed in Table I.

An important factor that has also been shown to affect the rate of onset and mixing is the buoyant crossover point between the stable and unstable regime, i.e. the mass fraction at which the fluid mixture becomes denser than the brine layer[35]. The crossover directly influences the time for a sufficiently dense boundary layer to accumulate and the subsequent maximal difference possible to provide the driving force. In this case, the cross over point and the maximum density for the MEG and BEG match closely (detailed in Table I) indicating that any observed differences should be a consequence of the viscosity contrast. In fact, all other parameters which would affect the mixing behavior were kept constant such as the permeability and the layer thickness/ratio of

the height of the MEG/BEG layer, H_T, to the brine layer, H_B.

The viscosity of the pure solutions and the mixtures were characterized using a Thermo Scientific Haake Mars 60 Modular Advanced Rheometer System equipped with double gap geometry. The fluids underwent two shear rate controlled tests at 20°C, sweeping stepwise from 200-10 s^{-1}, and then upwards from 10-200 s^{-1}, in increments of 10 s^{-1}. Each datum point was measured for 30 s, with 20 data points being collected per shear rate sweep. The shear stress and viscosity data were collected using the Haake RheoWin software and the fluids exhibited Newtonian behavior. The viscosity values were averaged over the entire shear rate range to obtain an absolute viscosity value for each fluid. The resulting viscosity curves are shown in Figure 1 as a function of wt% MEG/BEG, w_M.

Unexpectedly, at a mass fractions of MEG = 0.8, a maximum in viscosity is observed. Usually such curves follow concave, convex or step-wise transitions viscosity[20], however here we measure a peak which has so far not been reported in the literature nor has the effect been investigated concerning the problem of convective mixing. In the case of BEG, the viscosity curve is again non-linear. However, a maximum was not observed and instead a smooth concave transition was measured.

The Rayleigh number, *Ra*, Eq 1, is used to parameterize convective mixing. It provides a measure of the vigor of convection.

$$Ra = \frac{\kappa \Delta\rho_{\max} H_{\mathrm{B}} g}{\mu_2 \phi D_m} \tag{1}$$

where the permeability, κ is estimated using the Kozeny-Carmen equation with a porosity $\phi = 0.36$ so that $\kappa = 1.9 \times 10^{-10}$ m^2, gravitational acceleration, $g = 9.81$ m/s^2, the length scale is the height of the brine layer, $H_{\mathrm{B}} = 10$ cm, the average diffusion coefficient in the bulk solution $D_m = 1 \times 10^{-9}$ m^2/s, the viscosity of the bottom fluid is μ_2 and the maximum density difference is $\Delta\rho_{max}$ which is calculated from the difference between the maximum density of the fluid mixture and the pure fluid density of the bottom layer (ρ_2). *Ra* for each fluid pair is presented in Table I and because it is a function of maximum density difference and does not take into account the viscosity ratio, the *Ra* are comparable.

The detailed experimental methodology followed here can be found in Liyanage et al., 2019. Briefly, a Universal Systems HD-350 X-ray CT was employed to image with a time resolution of about 10cm/min and spatial resolution of 0.5 mm x 0.5 mm x 2mm. The experimental vessel was a 3 L acrylic plastic bowl (a sketch is shown in Figure 2) packed with soda glass ballotini with

TABLE I. Characteristic of the density curves of the two solution pairs, namely maximum density difference between the two solutions ($\Delta\rho_{\max}/\rho_2$), weight fraction at maximum density ($w^{\max}$) and at neutral buoyancy w^0, the viscosity of the resident fluid, μ_2, the viscosity ratio, M and Ra

Solution	$\Delta\rho_{\max}/\rho_2$	$w^{\max}$	w^0	μ_2 $[m.Pas]$	M	Ra
MEG/brine	0.90%	0.50	0.88	1.090	0.290	4610
BEG/brine	0.85%	0.53	0.80	1.124	0.075	3900

a particle diameter of 0.4-0.5mm (SiLibeads®, supplied by VWR, UK). Initially, the bowl was wet-packed with beads and brine up to 90% of its volume, corresponding to height, $H_{\mathrm{B}} \approx 10$ cm. Separately a dense slurry of the organic solution and beads was prepared and poured on carefully ($H_{\mathrm{T}} \approx 3$ cm), and the first CT scan was taken shortly after. Scans were then taken regularly for up to 24 hours.

It is important to note that in the post-imaging analysis, the domain is separated into two regions, defined by the initial EG-water interface as highlighted in the sketch of the experimental vessel in Figure 2. Each section is treated with independent calibration curves based on the average CT unit of all the voxels in the region below the initial interface $\widehat{CT}_{\mathrm{B}}$ or above the initial interface, $\widehat{CT}_{\mathrm{T}}$ at the initial and final time (t_0 and t_{f}). Then on a voxel-by-voxel basis, i, using Equation 2 the raw, time-dependent CT unit $CT_i(t)$ is converted into a physical quantity of the mass fraction, $w_{\mathrm{B},i}(t)$ or $w_{\mathrm{T},i}(t)$. The resulting data set can be either fully or partially reconstructed to provide visual insights into the mixing patterns and macroscopic quantities such as change of mass, and the dissolution rate can be calculated.

$$w_{\mathrm{B},i}(t) = \widehat{w}_{\mathrm{B}}(t_{\mathrm{f}}) \frac{CT_{\mathrm{B},i}(t) - CT_{\mathrm{B,i}}(t_0)}{\widehat{CT}_{\mathrm{B}}(t_{\mathrm{f}}) - \widehat{CT}_{\mathrm{B}}(t_0)} \tag{2a}$$

(2b)

$$w_{\mathrm{T},i}(t) = 1 - \frac{CT_{\mathrm{T},i}(t) - CT_{\mathrm{T}}(t_0)}{\widehat{CT}_{\mathrm{T}}(t_{\mathrm{f}}) - \widehat{CT}_{\mathrm{T}}(t_0)} \tag{2c}$$

III. RESULTS AND DISCUSSION

A. Onset of Convection and Dissolution Rate

Two experiments were performed with the BEG-water system, and these are compared to previously published data of experiments using MEG[10]. The domain is divided into two sections and the mass fraction of MEG/BEG is computed in the respective sections; the full methodology can be found in Liyanage et al,. 2019. The resulting MEG/BEG fraction dissolved in brine, m_j/M_1 is plotted as a function of the square root of time, $t^* = \sqrt{t}$ for each of the subdomains, top (closed symbols) and bottom (open symbols) in Figure 2 for MEG (black) and BEG (repeats are shown in red and blue). A modified logistic function is fitted to the data, and the pure diffusive case, calculated from a numerical solution of the one-dimensional diffusion equation in a sphere[10], is plotted.

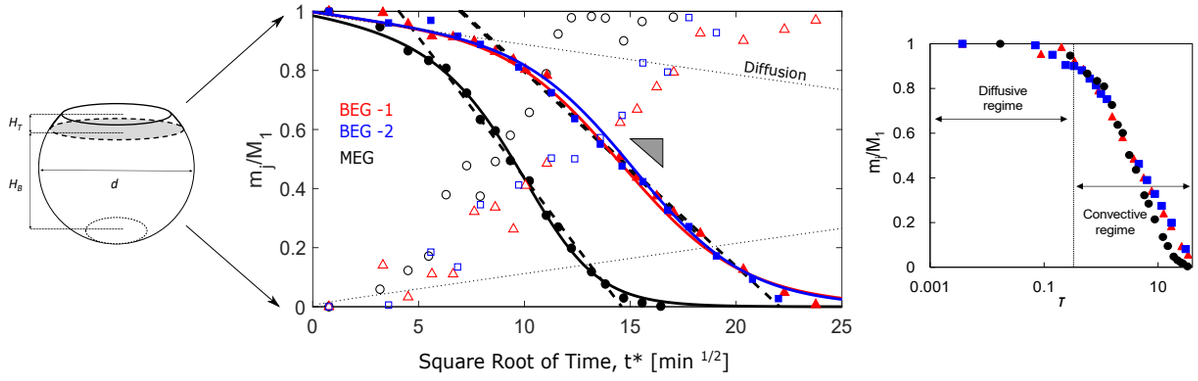

FIG. 2. Left: A sketch of the experimental vessel indicating the diameter, d, and the height of the bottom section initially containing brine, H_B and the height of the top section initially containing MEG or BEG, H_T. Middle: Relative mass of MEG/BEG dissolved in brine, m_j/M_1, as a function of the square root of time, $t^* = \sqrt{t}$ for experiments conducted with BEG-1 (blue), BEG-2 (red) and MEG (black). Filled and empty symbols refer to observations on the top (filled) and bottom (empty) sections of the bowl. The data is fitted with a modified logistic functions and a black dashed line indicates the linear region. Right: Relative mass for the top layer plotted as a function of dimensionless time, τ

First, we note a good agreement between the two BEG experiments and a similar trend between the MEG and BEG solutions. At early times ($t^* < 1-5$ min$^{0.5}$) all the experiments approached

the behavior predicted by a purely diffusive case. After which, as reported in Liyanage et al,. 2019 the rate of mass removal from the top layer linearly scales with the square root of time. A linear scaling of the growth of the mixing zone, in this case the finger propagation, with the square root of time has been utilized in previous works to describe the effect of hydrodynamic dispersion[23–25,36]. The gradient of this region is also an indication of the real-time progression of this process.

Thus, the onset and shutdown time can be estimated from the intersection of the linear region with a mass fraction of 1 (onset) or 0 (shutdown). The onset time for BEG (49±10 min) was 33 min slower than MEG (17±8 min) and the shutdown time for BEG (482±51 min) was 200 min slower than the MEG (202±47 min). The time for shutdown consistently occurs after we observe the fingers have reached the bottom of the domain.

A given time, t, can be converted to a dimensionless time, τ, via Eq 3[9,32]. For the onset time, the pure fluid viscosity of either MEG or BEG is used and $\mu = \mu_1$. The onset times converge so that for BEG $\tau = 0.11$ and $\tau = 0.18$ for the MEG. Interestingly, although these values are very similar the onset time for BEG is slightly earlier than MEG. Previously, it has been reported that the onset time of instability has a strong positive correlation to the mobility ratio[32]. So, as the viscosity contrast (μ_2/μ_1) increases the dimensionless onset time increases. There[32], numerical modeling investigated a wide range of viscosity ratios with and without a non-monotonic mixing profile between the fluids and concluded, contrary to the intuition that a strong viscosity contrast results in a more stable layer, that result showed that buoyant forces become more dominant with a decreasing mobility ratio.

$$\tau = t\frac{\kappa\Delta\rho_{\max}g}{\mu H_{\mathrm{B}}\phi} \tag{3}$$

Using the same non-dimensionalization but such that μ is equal to the mixture viscosity μ_{mix} at a given t, the change of mass curves for the MEG and BEG collapse into a single curve shown in Figure 2 (right). The onset of convection is approximated with a vertical dotted line so that a diffuse and convective regime can be observed before and after. It should be noted that only the curves for the top layer are shown but clearly display that it is the viscosity contrast controlling changes in behavior.

Next, the rate of convective dissolution, r, which represents the rate at which material is removed from the top layer, is calculated from the differential of the solid smooth curve fitted to the change of mass shown in Figure 2. The convective dissolution rate plotted with respect to time is presented in Figure 3a for the two BEG experiments (solid red and blue) and the MEG

experiment (solid black) the shaded regions represent an ensemble of numerical realizations to account for error in the raw data, also the diffusive case is plotted for comparison. It can be noted in Figure 3a that there is excellent agreement between the curves for the two BEG experiments. As observed before, the curves initially follow the trend predicted by the diffusion model until it reaches a maximum $r_{\max} = 0.29 \pm 0.06$ g/min (BEG-1, at 190 min) and $r_{\max} = 0.30 \pm 0.07$ g/min (BEG-2 at 180 min) before rapidly decreasing at late times. Compared to the MEG case where $r_{\max} = 0.61 \pm 0.06$ g/min (MEG at 74 min), the maximum dissolution rate is half for the BEG case.

However, the time to reach the maximum dissolution rates is approximately four times larger than the time required for the onset of convection for both the MEG (t($r_{\max}$)≈4.3t_c) and BEG (t($r_{\max}$)≈3.7t_c). There is also consistency in the magnitude of the increase in the dissolution rate relative to the rate at the onset of convection, r_{onset}. At the onset of convection for the MEG $r_{\text{onset}} = 0.40 \pm 0.03$ g/min and for the BEG $r_{\text{onset}} = 0.18 \pm 0.06$ g/min. So, in both cases the maximum rate of dissolution is a factor of approximately 1.5 larger than the rate at onset. Therefore, we observe that the relative increase in the rate is consistent.

To explain this observation we examine the fluid properties. At the time of the maximum flux, the mass fraction of MEG/BEG in the top and bottom regions is equivalent i.e. $w_i = 0.5$ at which point and thereafter, there is a convergence in both the viscosity and density profiles. It, therefore, follows that similar macroscopic properties, such as the relative magnitude of the dissolution rate and the shutdown time would be observed, albeit delayed with respect to the onset time. In these experiments a constant regime is not observed. Whilst it may be the case the fingers reach the bottom before this happens, a lack of a constant flux was predicted from numerical simulations for $Ra < 10^4$[41,7,37]. Therefore, to compare cases, the maximum dissolution rate is used[9,38].

The mass transport in the MEG and BEG system can be quantitatively compared using the Sherwood number *Sh*; which is essentially a comparison of convective transport in the form of the mass transport coefficient, k_m, to the diffusivity (D_m) over a given length scale, H, as Equation 4 and can be estimated directly from the ratio of the maximum convective dissolution rate to the corresponding value in the presence of diffusion alone, while accounting for the appropriate length scales, i.e.

$$Sh = \frac{k_m H}{D_m} = \frac{l_{\text{H}}}{l_D} \frac{(dm_{\text{T}}/dt)_H}{(dm_{\text{T}}/dt)_D} \tag{4}$$

where $l_{\text{H}} = 10$ cm $\approx H_{\text{B}}$ is the characteristic length scale of convective mixing, while l_D is the

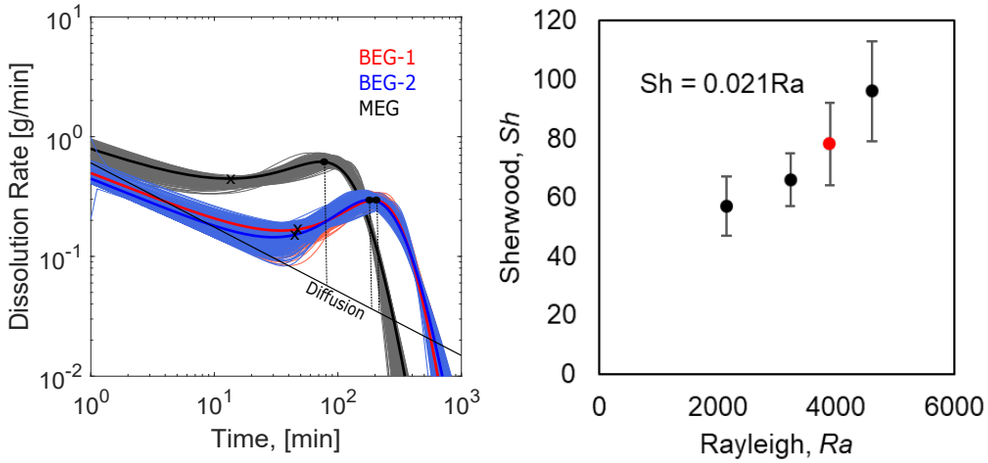

FIG. 3. left: Rate of dissolution as a function of time for the experiments conducted with BEG-1 (blue), BEG-2 (red) and MEG(59) (black). The solid colored lines are obtained upon differentiating the modified logistic function fitted to the experimental data (Figure 2), while the thin solid black line is the numerical solution of the purely diffusive scenario. The cross symbols indicate the time of the onset of convection (estimated from Figure 2), while the circles represent the time of the maximum rate of dissolution. Right: Sherwood number, *Sh* as a function of the Rayleigh number, *Ra*. Previously published data from a study using MEG[10] is reported (black symbols) alongside the current BEG study (red symbol) with the equation for a linear trend.

corresponding value associated with the diffusive process. Here, the latter has been chosen to be an estimate of the thickness of the diffusive boundary layer at the given time and take the value $l_D \approx 1-2$ cm depending on the system considered.

In the BEG system $Sh = 78 \pm 17$ and $Sh = 77 \pm 18$ respectively and $Sh = 94 \pm 19$ for the MEG. When plotted alongside the data from Liyanage et al., 2019 the BEG experiments fit well into the positive trend between $Sh - Ra$ as observed in Figure 3b.

In the low Ra range ($Ra_c < Ra < \mathcal{O}(Ra) \sim 10^3$), we expect a linear scaling (reflected in the original relationship from Liyanage et al., 2019) while flux is expected to become independent of Ra for $Ra > \mathcal{O}(Ra) \sim 10^4$[37,39,40]. Previous works using MEG or PG have observed a power-law relationship between Ra and Sh however these are typically reported with very large uncertainties in the parameters and the experiments are conducted at larger Ra. The current results, therefore, are not incompatible with the scaling proposed from experiments using similar fluid pairs (i.e.

Neufeld et al. 2010) but represent the phenomena in a different Ra range. Here, we observe a linear Sherwood-Rayleigh relationship, $Sh = 0.021Ra$ which is consistent with the original relationship from Liyanage et al., 2019 where $Sh = 0.025Ra$. So, although the onset of convection is later, the relative magnitude of the flux (to the diffusive) is not affected, indicating the buoyant effects are the dominant driving forces in this process.

B. Plume dynamics and flow structure

From the results presented thus far it would appear the two cases are consistent in their scaled time behavior. However, these similarities end at the macro-scale as the plume dynamics are vastly different between the two cases. We present both the averaged vertical profiles of the mass fraction of solute, w_M, in Figure 4 and 3D reconstructions of the two cases for qualitative comparisons in Figure 5. For both Figure 4 and Figure 5 time has been non-dimensionalized using Eq 3.

The differences in the plume structure can be inferred from concentration profiles which are plotted in Figure 4. The early times (red) to late times (blue) are shown for the two systems investigated, MEG (left) and BEG (right). Each point represents the average of all voxels in each 2 mm-thick horizontal section of the bowl; however, due to image noise at the interface, points within the grey box have been removed for clarity. In each plot, the solid black line represents the position of the interface at the start of the experiment.

For the MEG there is a spatially non-uniform concentration of solute towards the top of the bowl at early times (red curves) and an accumulation of material at the bottom of the bowl at late times (blue curves). In contrast, in the BEG case as there is no observed bulging of the concentration profile. Instead there is a trend towards a more evenly distributed low concentration plume spread out throughout the length of the domain resembling what would be expected from a purely diffusive case.

To look more closely at the evolution of the individual finger structure over time Figure 4 also shows horizontal 2D reconstructed cross sections of the MEG and BEG experiments at three locations in the bowl corresponding to position A ($\approx$ 3.4cm from top at $\tau \approx 0.2$), B ($\approx$ 7.6cm from top at $\tau \approx 5$) and C ($\approx$ 11.2cm from top at $\tau \approx 20$) as labeled on the concentration profiles. The color of the letter indicates the time during the experiment, and we first observe that for each time there are striking structural differences between the two cases. At position A, there are fewer fingers in the BEG case compared to the MEG; there are no isolated islands which would indicate

independent finger growth and instead a single large connected structure is visible. Fewer fingers form compared to the MEG case where many small fingers form across the entire cross-section.

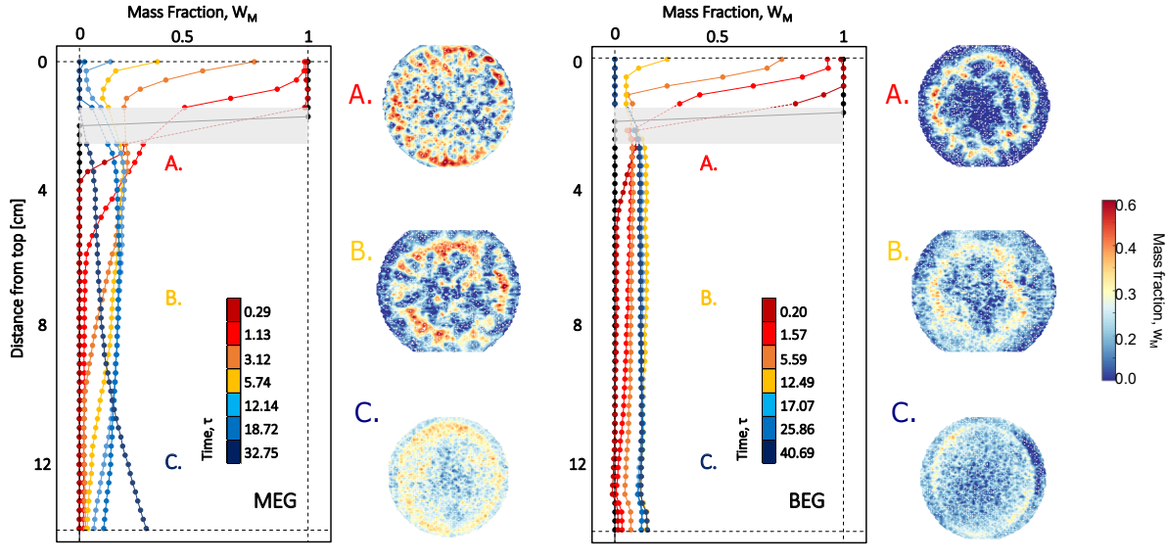

FIG. 4. Horizontally averaged profiles of the MEG (left) and BEG (right) mass fraction, w, as a function of the distance from the top of the bowl for various dimensionless times, τ. On the right of each profile are three horizontal, reconstructed cross-sections at three locations and times during the experiment; the letter color indicates the timing and the position of the letter indicates the location so that: A is a slice taken 3.4 cm from top at $\tau \approx 0.2$, B is taken 7.6 cm from top at $\tau \approx 5$ and C is 11.2 cm from top at $\tau \approx 20$.

At position B the concentration profiles show a similar average mass fraction of about 0.3. However, the spatial distribution of the solute is completely different. A ring structure has formed in the MEG case and continues to dominate in the BEG. However, in the MEG case, the concentration within the fingers remains high, and well-defined finger boundaries are visible. In the BEG case, the concentration gradients were not sharp, and lateral mixing of the fingers can be observed, as a result of the slower progression of the plume in real time allowing for greater dispersion.

At position C for the MEG there is a relatively uniform concentration of solute, and this is a result of the accumulation observed in the concentration profile. In the BEG case, the reconstruction also reveals a uniform concentration map however the average concentration is lower because the solute is evenly spread across the entire domain instead of slumped at the bottom. This suggests that overall, the mixing was better in the BEG case compared to the MEG.

Considering now Figure 5. Here is shown 3D reconstructions for MEG and BEG at the same

dimensionless time but it is clear the flow characteristics are not the same between the two cases. Similar to the observations in Figure 4, in both fluid pairs the interface recedes as fingers form and propagate through the bottom domain until a final mixing state is achieved; the similarity between the MEG and BEG is restricted to the amount of the top layer which has been dissolved. The spatial and temporal distribution of the solute in the bottom section is vastly different. In the MEG experiment the fingers are well defined and many individual fingers can be observed. In the BEG case the fingers are not well defined and there are less fingers than in the corresponding MEG case. The most surprising observation perhaps is that the fingers invade further in the BEG than the MEG. Given the *Ra* is slightly lower for the BEG and the viscosity is higher than the MEG, the opposite behavior would be predicted. Initially, in Figure 5 the flow appears to adhere to that expectation, however, by the second frame at $\tau = 1.13 - 1.57$ in the BEG, the fingers are longer and have penetrated further into the domain compared to the MEG.

Therefore, observations from the 3D reconstructions in Figure 5 can explain the flatter BEG concentration profile. At $\tau = 3 - 5$ the BEG fingers have penetrated further into the domain than the MEG. However, the fingers are less concentrated and are less well-defined which indicates more dispersion has occurred, and the result of high transverse and longitudinal dispersion is the quick reduction and flattening of the concentration gradients[38]. This result is consistent with previous numerical works where it has been shown that the larger the mixing zone, the closer the fingering phenomenon behaviors like a purely dispersive system[23]. As a result of an increase in dispersion the finger width is predicted to be larger and there be an increase in vertical spreading[43] both of which are observed in the BEG case. This observation agrees with the concentration profiles and reconstructions presented here where we see a smooth transition in the BEG case without the buildup of material, emblematic of the MEG case.

To quantify these observations we look to the role of dispersion. In a recent paper, a dispersive Rayleigh number is defined, $Ra_d = rH/d_p$, where H is the height and d_p the particle size and r is the ratio of longitudinal and transverse dispersivity, which can be assumed to be on the order ≈ 10 in bead pack[44]. By comparing Ra_d to the molecular (conventional) Rayleigh number so that $D = Ra_d/Ra$ results in a criterion for when dispersion is and is not dominant; when $D << 1$ dispersion is dominant. In this case, $D = 0.43$ for MEG and $D = 0.51$ for BEG which is within the range reported previously 0.0011 - 0.74[44] indicating that dispersion is important in these systems.

Now, to calculate the transverse dispersion coefficient, D_t, we use two methods 1) using domain averaged quantities [45,46] and 2) using finger properties[9,41]. For the first method, the spatial vari-

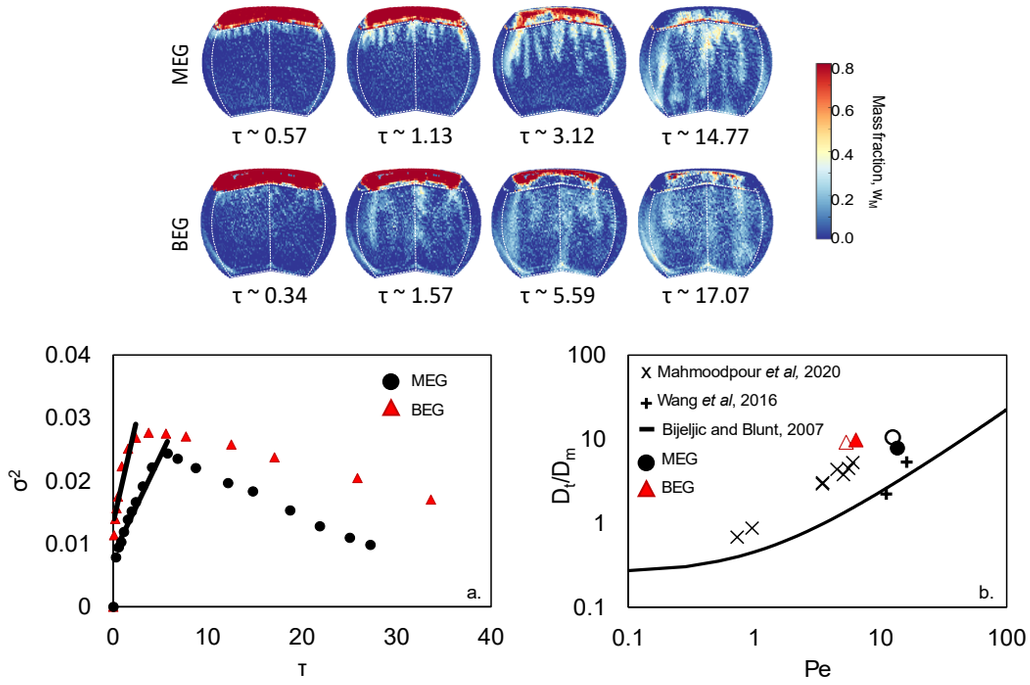

FIG. 5. Top: 3D reconstructions of the bowl, MEG (top) and BEG (bottom), in terms of mass fraction, w, for various dimensionless times, τ. Bottom: a. Time evolution of the spatial variance of the concentration field for MEG and BEG where the black line indicates the region used for the calculation of the transverse dispersion coefficient. b. D_t/D_m vs Pe for the MEG and BEG using the two methods; domain averaged (filled points) and finger averaged (open points) compared to previously reported data for MEG system[9](plus symbol), CO_2-brine system [41](cross symbol), and the solid line is pore-scale modelling of uniform flow[42].

ance, σ^2, of the concentration field of each horizontal slice is averaged across the whole domain for each time. The result is plotted as a function of dimensionless time for the MEG and BEG and is shown in Figure 5. As expected the variance increases over the course of the experiment as the MEG or BEG mixes with the brine before decreasing again as the domain homogenizes towards the final concentration. The variance for the BEG increases faster than the MEG indicating that the plume is subject to more lateral spreading. However, the decrease in the variance is faster for the MEG than the BEG indicating that the MEG reached a final mixing state at a faster rate. Observing the 3D plume directly confirms the structural differences in flow patterns which influence the evolution of the variance; indeed, the larger fingers in the BEG case undergo more spreading throughout the experiment, resulting in a higher variance.

Then to calculate D_t, the change in σ^2 across the initial increase, as indicated with a black line

in Figure 5, with respect to dimensional time is used according to Equation 5.

$$D_t = \frac{1}{2}\frac{d\sigma^2}{dt} \tag{5}$$

The second method for calculating D_t is given in Equation 6 and uses individual finger properties, such as the change in concentration across the radius of the finger, $\partial C/\partial r$, and the change in concentration along the length of the finger, $\partial C/\partial z$, along with the fingertip speed, U_f, which is calculated by tracking the finger location from one time to another, and finger radius, r_f.

$$U_f r_f \frac{\partial C}{\partial z} = 2D_t \frac{\partial C}{\partial r} \tag{6}$$

The resulting D_t of each method for the MEG and BEG is shown in Table II. In general there is a good agreement between the two methods for each case. Also shown in Table II is the Péclet number, *Pe*, for each case which is defined as the ratio between the time needed for the solute to travel a characteristic length by diffusion compared to the time needed by advection. In a porous medium and for this problem, *Pe* can be defined as $Pe = Ud_p/\phi D_m$[9,41,42]. For Method 1, U is the front propagation velocity calculated from the onset and shutdown times of the MEG and BEG and is consistent with the fingertip speed measured from the images as shown in Table II. Thus, it is observed that the BEG progresses 2-3 times slower than the MEG and this is can be solely attributed to the mobility ratio. As the U is consistent between the methods, the resulting *Pe* for each method is comparable, but between the MEG and the BEG, *Pe* is approximately half.

TABLE II. Result of the calculation of the transverse dispersion coefficient, D_t using method 1 and 2, the normalized D_t with the diffusion coefficient, $D_m = 1 \times 10^{-9}$ and the *Pe* calculated from U which is the front propagation speed in Method 1 or the fingertip velocity in Method 2.

	U	D_t	D_t/D_m	Pe
	$[m/s]$	$[m^2/s]$	-	-
MEG Method 1	9.01×10^{-6}	1.05×10^{-8}	10.5	12.5
MEG Method 2	9.80×10^{-6}	7.81×10^{-9}	7.81	13.6
BEG Method 1	3.85×10^{-6}	9.19×10^{-9}	9.19	5.35
BEG Method 2	4.60×10^{-6}	9.76×10^{-9}	9.76	6.39

Finally, in Figure 5b we plot the dispersion coefficient normalized by diffusion, D_m, with

respect to the *Pe* for each case and compare this to other previously published data from convective dissolution experiments, at similar *Ra*, using a similar fluid pair MEG-NaI-brine with $Ra = 3360 - 5010$[9] and CO_2-brine system with $Ra = 3272 - 4841$[41], together with pore-scale modeling for uniform flow[42].

From this previously reported data, the transverse dispersion coefficient is constant at $Pe < 1$ where dispersion is not dominant and increases as a power-law function for $1 < Pe < 300$. Interestingly, between the MEG and BEG cases we do not observe an increase in D_t with *Pe*, instead dispersion remains constant. In addition, the dispersion reported in the BEG is almost one order of magnitude larger than expected from the uniform flow simulations. As a result, this clearly suggests greater dispersion and hence more mixing has occurred than expected.

The question of why more dispersion is observed than expected in a fluid pair with a high viscosity contrast may be explained with a comparison of the finger propagation speed to the interstitial velocity, $U^* = \kappa \Delta \rho g / \mu_1$. In the BEG case, $U/U^* = 3.7$ compared to 1.8 for the MEG, indicating that the front is progressing faster than the buoyant velocity, resulting in a greater shear at the finger-brine interface.

Although the data from the current study is limited it suggests the *Pe* and D_t for the MEG is similar to that reported for similar fluid pairs. However, compared to the CO_2-brine system, in general there is a higher *Pe* and dispersion in the analog fluid pairs. More data from analog fluid experiments in this low *Pe* range would be needed to confirm this observation, however, it raises an important implication for comparisons between the experiments and the field. Reliable estimates from the laboratory are critical to understanding the movement and long-term trapping of CO_2 in saline aquifers.

IV. CONCLUSION

Here, we show that a strong viscosity contrast is changing fluid-fluid interactions responsible for the onset of convective mixing and resulting in significant alterations to flow dynamics. The commonly used MEG-water system is compared with a new fluid, BEG-water, which exhibits a similar density profile but with a viscosity contrast 4 times larger than MEG-water. It was observed that the onset and shutdown time of convection was 2-3 times longer for the more viscous fluid, but other macroscopic measures, such as the relative magnitude of the rate of mass transfer, remain unaffected.

However, there is significant dissimilarity in the spatial evolution of the dissolved plume between the two cases. Using 3D reconstructions we compared the finger structures and observed larger, fewer and less concentrated fingers that penetrate further into the domain in the BEG case compared to the MEG. So although the same amount of material has moved from the initial top layer to the bottom layer, between the two cases we observed that the material could either stay in small, highly concentrated fingers close to the initial interface (MEG) or extend much further down into the domain in large. low concentration fingers (BEG) due to greater dispersion. This result is contradictory to previous insights which suggest the fingers should be fewer and shorter with a larger viscosity ratio or smaller *Ra* but support studies which focus on the importance of dispersion in fluid-fluid mixing.

The finger structures were quantified using horizontal concentration profiles where it became clear that the BEG case closely resembles the pure diffusive case, where the concentration profile is flat throughout the experiment. To explain this observation we suggest that as a result of a larger viscosity contrast more lateral mixing occurs and this ultimately results in more dispersion and a better mixed system. The implication of this observation is that the fluid properties have a fundamental and far reaching effect on the nature of the flow and the final mixing state. This conclusion is not by itself surprising but becomes important when these analog fluids are used for inferring large scale behavior.

Convective mixing is an important mechanism in carbon storage where the trajectory of the dissolved plume and the eventual mixing state are essential to ensuring long term security and estimating the trapping potential of a given site. However, given the sensitives shown here the true nature of 3D mixing may be different to that shown using analog fluids. In this study, due to an order of magnitude difference in mobility ratio, M we observe significant changes in plume structure and mixing behaviors between the MEG and BEG. It is reasonable then to suggest that there would also be differences between the MEG/water system ($M \approx 0.29$) and the CO_2-rich brine/brine ($M \approx 1$) which also exhibits an approximately similar difference in M. This study, therefore, is a reminder that accurate experimental data is required in order to predict subsurface behavior, and, more broadly that fluid-fluid interactions are extremely sensitive such that basic characterization should not be overlooked.

ACKNOWLEDGMENTS

This work was performed as part of the PhD thesis of Rebecca Liyanage, funded by a departmental scholarship from the Department of Chemical Engineering, Imperial College London, provided by EPSRC (Award Ref. 1508319). Andrew Russell thanks the UK Engineering and Physical Sciences Research Council (EPSRC, Award Ref. 18755724) and Syngenta Ltd for the funding of this work. Experiments were performed in the Qatar Carbonates and Carbon Storage Research Centre at Imperial College London, funded jointly by Shell, Qatar Petroleum, and the Qatar Science and Technology Park. The data that support the findings of this study are openly available in UKCCSRC data repository (Data set ID 13607381) or the data that support the findings of this study are available from the corresponding author upon reasonable request.

REFERENCES

[1]H. Emami-Meybodi, H. Hassanzadeh, C. P. Green, and J. Ennis-King, "Convective dissolution of CO_2 in saline aquifers: Progress in modeling and experiments," International Journal of Greenhouse Gas Control (2015), 10.1016/j.ijggc.2015.04.003.

[2]S. M. Benson and F. M. Orr, "Carbon dioxide capture and storage," MRS Bulletin **33**, 303–305 (2008).

[3]H. E. Huppert and J. a. Neufeld, "The Fluid Mechanics of Carbon Dioxide Sequestration," Annual Review of Fluid Mechanics **46**, 255–272 (2014).

[4]Nazari-Moghaddam, Rasoul, Rostami, Behzad, Pourafshary, and Peyman, "Scaling analysis of the convective mixing in porous media for geological storage of co_2: An experimental approach," Chemical Engineering Communications **202**, 815–822 (2015).

[5]J. A. Neufeld, M. A. Hesse, A. Riaz, M. A. Hallworth, H. A. Tchelepi, and H. E. Huppert, "Convective dissolution of carbon dioxide in saline aquifers," Geophysical Research Letters **37** (2010), 10.1029/2010GL044728.

[6]S. Backhaus, K. Turitsyn, and R. E. Ecke, "Convective instability and mass transport of diffusion layers in a Hele-Shaw geometry," Physical Review Letters **106**, 1–4 (2011).

[7]A. C. Slim, M. M. Bandi, J. C. Miller, and L. Mahadevan, "Dissolution-driven convection in a hele–shaw cell," Physics of Fluids **25** (2013), 10.1063/1.4790511.

[8]E. Agartan, L. Trevisan, A. C. J., B. Q. Zhou, and T. Illangasekare, "Experimental study on

effects of geologic heterogeneity in enhancing dissolution trapping of supercritical co_2," Water Resour. Res **51** (2015), 10.1002/2014WR015778.

[9]L. Wang, Y. Nakanishi, A. Hyodo, and T. Suekane, "Three-dimensional structure of natural convection in a porous medium: Effect of dispersion on finger structure," International Journal of Greenhouse Gas Control **53**, 274–283 (2016).

[10]R. Liyanage, J. Cen, S. Krevor, J. P. Crawshaw, and R. Pini, "Multidimensional observations of dissolution-driven convection in simple porous media using x-ray ct scanning," Transp Porous Med **126**, 355 – 378 (2019).

[11]T. J. Kneafsey and K. Pruess, "Laboratory flow experiments for visualizing carbon dioxide-induced, density-driven brine convection," Transport in Porous Media **82**, 123–139 (2010).

[12]S. Mahmoodpour, B. Rostami, M. R. Soltanian, and M. A. Amooie, "Effect of brine composition on the onset of convection during co2 dissolution in brine," Computers & Geosciences **124**, 1 – 13 (2019).

[13]S. Mahmoodpour, B. Rostami, M. R. Soltanian, and M. A. Amooie, "Convective dissolution of carbon dioxide in deep saline aquifers: Insights from engineering a high-pressure porous visual cell," Phys. Rev. Applied **12**, 034016 (2019).

[14]Y. Tang, Z. Li, R. Wang, M. Cui, X. Wang, Z. Lun, and Y. Lu, "Experimental study on the density-driven carbon dioxide convective diffusion in formation water at reservoir conditions," ACS Omega **4**, 11082–11092 (2019), https://doi.org/10.1021/acsomega.9b00627.

[15]M. McBride-Wright, G. C. Maitland, and J. P. M. Trusler, "Viscosity and density of aqueous solutions of carbon dioxide at temperatures from (274 to 449) k and at pressures up to 100 mpa," Journal of Chemical & Engineering Data **60**, 171–180 (2015), https://doi.org/10.1021/je5009125.

[16]A. W. Islam and E. S. Carlson, "Viscosity models and effects of dissolved co2," Energy & Fuels **26**, 5330–5336 (2012).

[17]P. Saffman, "The penetration of a fluid into a porous medium or hele-shaw cell containing a more viscous liquid," Proceedings of the Royal Society of London A: Mathematical, Physical and Engineering Sciences **245**, 312–329 (1958), http://rspa.royalsocietypublishing.org/content/245/1242/312.full.pdf.

[18]G. M. Homsy, "Viscous fingering in porous media," Annual review of fluid mechanics **19**, 271–311 (1987).

[19]j. F. Orr and J. Taber, "Use of carbon dioxide in enhanced oil recovery," Science **224**, 563–569

(1984).

[20]B. Jha, L. Cueto-Felgueroso, and R. Juanes, "Fluid mixing from viscous fingering," Physical review letters **106**, 194502 (2011).

[21]I. Bihi, M. Baudoin, J. E. Butler, C. Faille, and F. Zoueshtiagh, "Inverse saffman-taylor experiments with particles lead to capillarity driven fingering instabilities," Phys. Rev. Lett. **117**, 034501 (2016).

[22]F. J. Hickernell and Y. C. Yortsos, "Linear stability of miscible displacement processes in porous media in the absence of dispersion," Studies in Applied Mathematics **74**, 93–115 (1986), https://onlinelibrary.wiley.com/doi/pdf/10.1002/sapm198674293.

[23]D. Loggia, N. Rakotomalala, D. Salin, and Y. C. Yortsos, "Evidence of new instability thresholds in miscible displacements in porous media," Europhysics Letters (EPL) **32**, 633–638 (1995).

[24]D. Loggia, D. Salin, and Y. C. Yortsos, "The effect of dispersion on the stability of non-monotonic mobility profiles in porous media," Physics of Fluids **10**, 747–749 (1998), https://doi.org/10.1063/1.869579.

[25]D. Loggia, N. Rakotomalala, D. Salin, and Y. C. Yortsos, "The effect of mobility gradients on viscous instabilities in miscible flows in porous media," Physics of Fluids **11**, 740–742 (1999), https://doi.org/10.1063/1.869943.

[26]O. Manickam and G. Homsy, "Simulation of viscous fingering in miscible displacements with nonmonotonic viscosity profiles," Physics of Fluids **6**, 95–107 (1994).

[27]M. Mishra, P. M. J. Trevelyan, C. Almarcha, and A. De Wit, "Influence of double diffusive effects on miscible viscous fingering," Phys. Rev. Lett. **105**, 204501 (2010).

[28]N. Sabet, H. Hassanzadeh, and J. Abedi, "Control of viscous fingering by nanoparticles," Phys. Rev. E **96**, 063114 (2017).

[29]B. Meulenbroek, R. Farajzadeh, and H. Bruining, "The effect of interface movement and viscosity variation on the stability of a diffusive interface between aqueous and gaseous co2," Physics of Fluids **25**, 074103 (2013), https://doi.org/10.1063/1.4813072.

[30]O. Manickam and G. M. Homsy, "Fingering instabilities in vertical miscible displacement flows in porous media," Journal of Fluid Mechanics **288**, 75–102 (1995).

[31]O. Manickam and G. M. Homsy, "Stability of miscible displacements in porous media with nonmonotonic viscosity profiles," Physics of Fluids A: Fluid Dynamics **5**, 1356–1367 (1993), https://doi.org/10.1063/1.858571.

[32]D. Daniel and A. Riaz, "Effect of viscosity contrast on gravitationally unstable diffusive layers

in porous media," Physics of Fluids **26**, 116601 (2014), https://doi.org/10.1063/1.4900843.

[33]M. C. K. Kim, "Onset of buoyancy-driven convection in a variable viscosity liquid saturated in a porous medium," Chemical Engineering Science **113**, 77 – 87 (2014).

[34]N. Sabet, H. Hassanzadeh, and J. Abedi, "A new insight into the stability of variable viscosity diffusive boundary layers in porous media under gravity field," AIChE Journal **64**, 1083–1094 (2018), https://aiche.onlinelibrary.wiley.com/doi/pdf/10.1002/aic.15974.

[35]H. Emami-Meybodi, "Stability analysis of dissolution-driven convection in porous media," Physics of Fluids **29**, 014102 (2017), https://doi.org/10.1063/1.4974275.

[36]Y. C. Yortsos and M. Zeybek, "Dispersion driven instability in miscible displacement in porous media," The Physics of Fluids **31**, 3511–3518 (1988), https://aip.scitation.org/doi/pdf/10.1063/1.866918.

[37]A. C. Slim, "Solutal-convection regimes in a two-dimensional porous medium," Journal of Fluid Mechanics **741**, 461–491 (2014).

[38]L. WANG, Y. NAKANISHI, A. D. TESTON, and T. SUEKANE, "Effect of diffusing layer thickness on the density-driven natural convection of miscible fluids in porous media: Modeling of mass transport," Journal of Fluid Science and Technology **13**, JFST0002–JFST0002 (2018).

[39]J. J. Hidalgo, J. Fe, L. Cueto-Felgueroso, and R. Juanes, "Scaling of convective mixing in porous media," Phys. Rev. Lett. **109**, 264503 (2012).

[40]J.-H. Ching, P. Chen, and P. A. Tsai, "Convective mixing in homogeneous porous media flow," Phys. Rev. Fluids **2**, 014102 (2017).

[41]S. Mahmoodpour, M. A. Amooie, B. Rostami, and F. Bahrami, "Effect of gas impurity on the convective dissolution of co2 in porous media," Energy **199**, 117397 (2020).

[42]B. Bijeljic and M. J. Blunt, "Pore-scale modeling of transverse dispersion in porous media," Water Resources Research **43** (2007), 10.1029/2006WR005700, https://agupubs.onlinelibrary.wiley.com/doi/pdf/10.1029/2006WR005700.

[43]Y. Xie, C. T. Simmons, and A. D. Werner, "Speed of free convective fingering in porous media," Water Resources Research **47** (2011), 10.1029/2011WR010555, https://agupubs.onlinelibrary.wiley.com/doi/pdf/10.1029/2011WR010555.

[44]Y. Liang, B. Wen, M. A. Hesse, and D. DiCarlo, "Effect of dispersion on solutal convection in porous media," Geophysical Research Letters **45**, 9690–9698 (2018), https://agupubs.onlinelibrary.wiley.com/doi/pdf/10.1029/2018GL079849.

[45]M. Boon, B. Bijeljic, and S. Krevor, "Observations of the impact of rock heterogene-

ity on solute spreading and mixing," Water Resources Research **53**, 4624–4642 (2017), https://agupubs.onlinelibrary.wiley.com/doi/pdf/10.1002/2016WR019912.

[46]M. Boon, B. Bijeljic, B. Niu, and S. Krevor, "Observations of 3-d transverse dispersion and dilution in natural consolidated rock by x-ray tomography," Advances in Water Resources **96**, 266 – 281 (2016).

[47]Y. C. Yortsos and M. Zeybek, "Dispersion driven instability in miscible displacement in porous media," The Physics of Fluids **31**, 3511–3518 (1988), https://aip.scitation.org/doi/pdf/10.1063/1.866918.